Supporting Information for

Charge Carrier Dynamics in 2D Hybrid Metal Halide Perovskites

Rebecca L. Milot, [†] Rebecca J. Sutton, [†] Giles E. Eperon, [†,§] Amir Abbas Haghighirad, [†] Josue Martinez Hardigree, [†] Laura Miranda, [‡] Henry J. Snaith, [†] Michael B. Johnston, [†] and Laura M. Herz[†,*]

† Department of Physics, University of Oxford, Clarendon Laboratory, Parks Road, Oxford, OX1 3PU, United Kingdom

‡ Oxford Photovoltaics Ltd., Unit 6 Begbroke Science Park, Woodstock Road, Oxford, OX5 1PF, United Kingdom

§ Present address: Department of Chemistry, University of Washington, Seattle, WA, USA

*Corresponding author: laura.herz@physics.ox.ac.uk

Contents

1. Additional experimental details

Materials

All materials were purchased from Sigma-Aldrich, Alfa Aesar or DyeSol and used as received unless stated otherwise.

Phenethylammonium iodide synthesis

PEAI (PEA = $C_6H_5(CH_2)_2NH_3^+$) was prepared in-house by modifying a previously detailed procedure for the synthesis of MAI by replacing methylamine with phenethylamine.[1]

Substrate preparation

Glass slides, coverslips, and quartz optical discs were cleaned sequentially in acetone and isopropanol, and then treated with oxygen plasma for 5 minutes immediately before film deposition.

Perovskite precursor solution and film preparation

PEAI (PEA = $C_6H_5(CH_2)_2NH_3^+$), MAI, and PbI_2 were dissolved in DMF in the appropriate molar ratios to give 1 M precursor solutions of $(PEA)_2PbI_4$ or $MAPbI_3$. The $(PEA)_2PbI_4$ and $MAPbI_3$ stock solutions were mixed in the respective ratios of 1:3, 1:2, and 1:1 by volume for films with mixed cations. To form perovskite films, the precursors were spin-coated in air or in a drybox (<20% RH) at 2000 rpm for 45 seconds and subsequently annealed at 70 °C for 10 minutes.

Film characterisation

Sample thicknesses were measured using a Veeco Dektak 150 surface profilometer. An Panalytical X'pert powder diffractometer with Cu anode X-ray source (Cu kα_1, 1.54060 Å) was used to obtain XRD spectra of films on glass.

Table S1. Film thicknesses

%PEA	Thickness (nm)
0	900
40	580
50	780
67	610
100	680

GIWAXS characterisation

GIWAXS studies were undertaken on Beamline I07 at the Diamond Light Source, UK, using a beam energy of 12.24 keV (λ = 1.0129 Å) focused with a 4-bounce Si(111) monochromator to a beam width of 100 μm. Samples were maintained in an opaque environmental chamber with Kapton windows, independently-controllable fore-beam knives and Pb beamstop. A 0.5 sccm He flow into the chamber ensured reduced incoherent ambient scattering. Images were acquired with a 4 s exposure time using a Pilatus 2M detector in rotated configuration. Sample-detector distance and beam energy were calibrated using a thermally-deposited 130 nm Ag layer and matched against ICDD card 00-004-0783, with the largest relative error and $\delta\mathbf{q}$ at $\mathbf{q}$=3.066 Å^{-1} of 0.002 and 0.008 Å^{-1}, respectively. The DAWNSci suite was used for data reduction.[2] Attenuation lengths were calculated using the online calculator which may be

accessed via the following hyperlink: http://henke.lbl.gov/optical_constants/atten2.html.[3] XRD patterns were calculated from simulated structures using the 3D visualization program VESTA.

UV-vis. measurements

The absorbance spectrum of $(PEA)_2PbI_4$ was taken using a Bruker Vertex 80v Fourier-transform infrared (FTIR) spectrometer with a tungsten halogen source and a silicon diode detector. The spectrometer was fitted with a transmission/reflection accessory, and spectra were taken in vacuum. Absorbance spectra for all of the other thin films were taken using a Varian Cary 300 UV-vis spectrophotometer with an internally coupled integrating sphere.

Time-resolved photoluminescence

For time-resolved PL, a picosecond pulsed diode laser (Picoquant, LDH-D-C-405M) centered at 405 nm was used to photoexcite the sample. The laser was set to a repetition rate of 10 MHz and fluence of 1.2 $\mu J/cm^2$. The PL was collected and directed toward a grating monochromator (Princeton Instruments, SP-2558) fitted with a photon-counting detector (PDM series from MPD). The timing was controlled with a PicoHarp300 time-correlated single photon counting (TCSPC) event timer. Time decay traces were recorded at the respective PL maxima for all of the samples.

Optical-pump THz probe spectroscopy

The output of an amplified laser system (Spectra Physics, Tsunami – Empower – Spitfire) with a repetition rate of 1.1 kHz, center wavelength of 800 nm, and pulse duration of 40 fs was used to generate THz radiation using optical rectification in a 450-μm thick GaP(110) crystal. This THz probe was then focused onto the sample and detected via free-space electro-optic sampling in a ZnTe crystal [0.2 mm ZnTe(110) on 3 mm ZnTe(110)]. A 400-nm pump pulse was generated using a BBO crystal. To record time-dependent decay traces, the change in peak THz amplitude was measured as a function of pump-probe delay time.

In conjunction with the THz measurements, in situ steady state PL spectra were collected using a UV-vis mini spectrometer (Ocean Optics, USB2000+) fitted with an optical fiber, a collimating lens, and a 435-nm long-pass filter.

2. THz Data Analysis

Charge-carrier mobility calculation

The charge carrier mobility μ is given by

$$\mu = \frac{\Delta S A_{eff}}{Ne}, \tag{S1}$$

where ΔS is the sheet conductivity of the perovskite thin film, A_{eff} is the effective area of the overlap of optical pump and THz probe pulse, N is the number of photoexcited charge carriers, and e is the elementary charge.

Assuming that the film thickness is much smaller than the THz wavelength, the sheet photoconductivity ΔS of a thin film between two media of refractive indices, n_{A} and n_{B}, can be expressed as[4,5]

$$\Delta S = -\varepsilon_0 c\left(n_A + n_B\right)\left(\frac{\Delta T}{T}\right), \tag{S2}$$

where $\Delta T/T$ is the experimentally determined change in transmitted THz electric field amplitude. In our experiment, $n_{\text{A}} = 1$ for vacuum and $n_{\text{B}} = 2.13$ for the z-cut quartz substrate.

The number of photo-excited charge carriers N can be determined using the following equation:

$$N = \varphi \frac{E\lambda}{hc}\left(1 - R_{pump}\right)\left(1 - T_{pump}\right), \tag{S3}$$

where E is the energy contained in an optical excitation pulse of wavelength λ, R_{pump} is the reflectivity of the sample at normal incidence of the excitation beam, T_{pump} transmittance of the pump beam, and φ is the ratio of free charge carriers created per photons absorbed (the photon-to-charge branching ratio).

Substituting Equations S7 and S6 into Equation S5, the following equation is obtained:

$$\varphi\mu = -\varepsilon_0 c\left(n_A + n_B\right)\frac{A_{eff} hc}{Ee\lambda\left(1 - R_{pump}\right)\left(1 - T_{pump}\right)}\left(\frac{\Delta T}{T}\right). \tag{S4}$$

Because $0 \le \varphi \le 1$, the effective mobility φμ represents a lower limit, which becomes identical to the actual mobility for full photon to free carrier conversion. To allow accurate determination of φμ, we ensured that excitation conditions were in the linear regime. It should also be noted that the determined charge carrier mobility arises from the contributions of both electrons and holes and that these contributions cannot be separated.

Fits to THz photoconductivity transients

As described in the main text, the overall recombination dynamics can be described by the following equation:

$$\frac{dn}{dt} = -k_3 n^3 - k_2 n^2 - k_1 n\,, \tag{S5}$$

where n is the charge-carrier density, k_1 is the monomolecular rate constant, k_2 is the bimolecular rate constant, and k_3 is the Auger rate constant.

As the experimentally observed quantity in optical pump-THz probe measurements, $\Delta T / T = x(t)$, is proportional to the photoconductivity, it is also proportional to the carrier density.

$$n(t) = \varphi C x(t) \tag{S6}$$

The photon-to-charge branching ratio φ indicates the fraction of absorbed photons which are converted to charge carriers. The proportionality factor $C = \tilde{n}_0 / x(0)$ is the ratio of the absorbed photon density $\tilde{n}_0$ to the initial THz response at time zero $x(0)$, where

$$\tilde{n}_0 = \frac{E \lambda \alpha(\lambda)}{hcA_{eff}} \left(1 - R_{pump}\right). \tag{S7}$$

The absorbed photon density is a function of the absorption coefficient α and reflectance R_{pump} of the sample at the excitation wavelength λ and of the effective overlap A_{eff} of the optical pump beam and THz probe beam. At high excitation fluences, $x(0)$ is no longer proportional to $\tilde{n}_0$. The value of C is therefore determined using a value of $x(0)$ within the regime where $x(0)$ is linearly proportional to the excitation fluence.

An expression for the time-dependent THz dynamics can be obtained by substituting Equation S2 into Equation S1:

$$\begin{aligned} \frac{dx}{dt} &= -C^2 \varphi^2 k_3 x^3 - C \varphi k_2 x^2 - k_1 x \\ &= -A_3 x^3 - A_2 x^2 - A_1 x \end{aligned} \tag{S8}$$

with $A_i = C^{i-1} \varphi^{i-1} k_i$. The coefficients A_1, A_2, and A_3 are determined via a global fit to a fluence dependent set of THz transients. As the photon-to-free-carrier conversion ratio φ is unknown, we can

only determine the values $\varphi^2 k_3$, φk_2 and k_1 from our fits. These equal the actual decay rate constants k_3, k_2 and k_1 in case the material exhibits full photon-to-free-charge conversion and are lower limits when $\varphi < 1$.

To account for the spatially varying charge density profile, the fit routine takes into account the exponential charge density profile created by the pump beam by dividing the sample into 50 equally thick slabs and computing the decay function for all of these individually.

3. Additional steady-state PL spectra

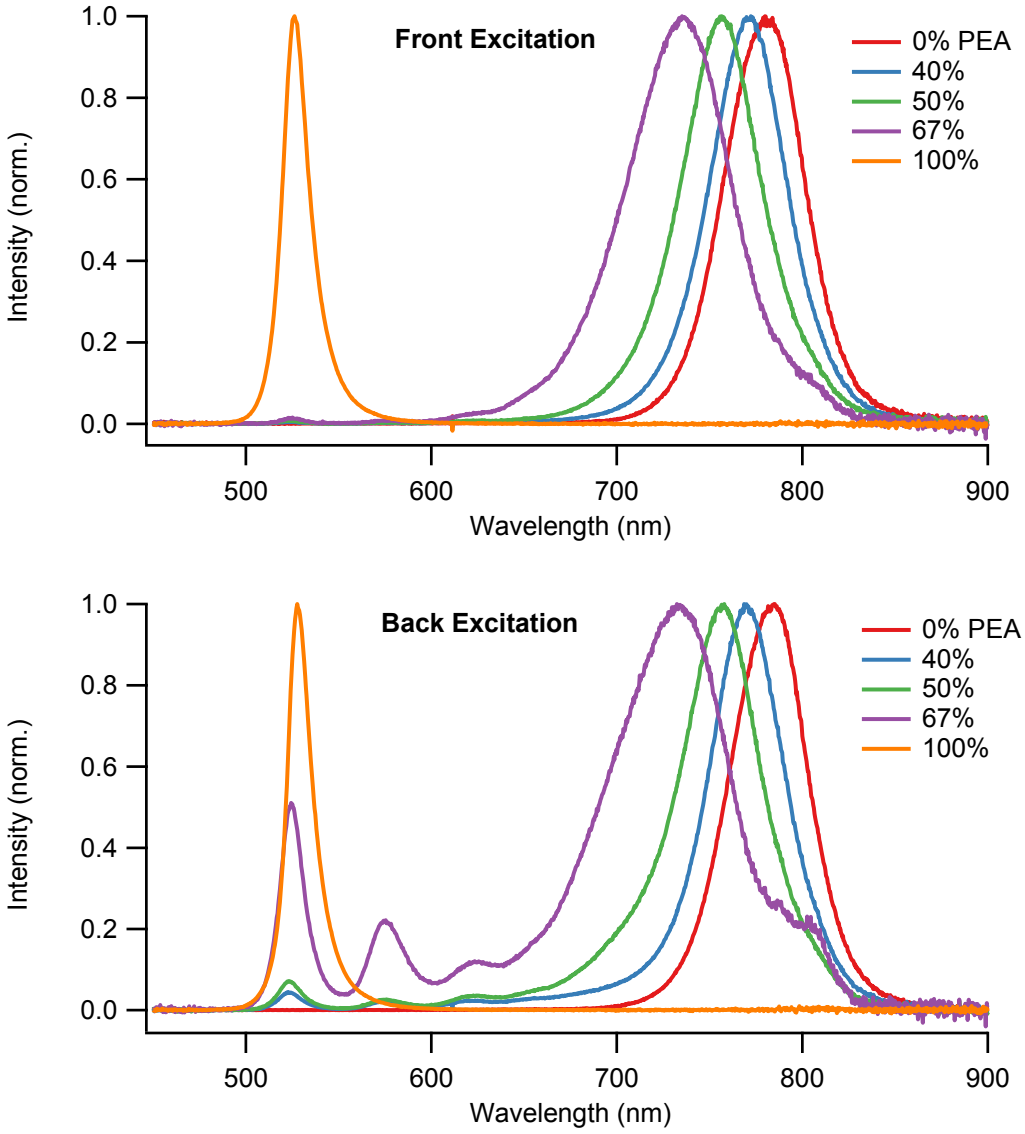

Figure S1. Comparison of steady-state photoluminescence spectra obtained following excitation at 400 nm and 63μJ/cm^2 with the perovskite thin film first (front excitation) and the quartz substrate first (back excitation). Film thicknesses were all greater than 550 nm (see SI), which is significantly larger that the optical absorption depth at the 400nm excitation wavelength (less than 100nm for all films).

4. Time-resolved PL

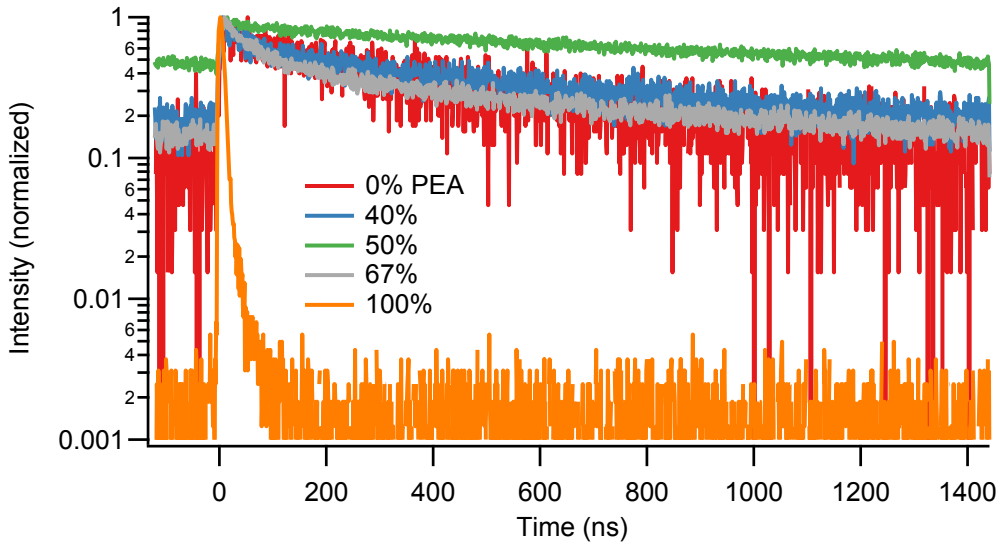

Figure S2. Time-dependent photoluminescence. The samples were photoexcited at 405 nm with a fluence of 1.2 μJ/cm^2. Traces were taken monitoring the decay at the respective photoluminescence peaks of the various samples.

5. GIWAXS Data and Analysis

Analysis of $(PEA)_2PbI_4$ GIWAXS data

In Figure S3 we present GIWAXS patterns for the $(PEA)_2PbI_4$ film, for grazing incidence angles of 0.05°, 0.19° and 0.50°. The Debye-Scherrer rings are broken into sharp spots of intensity which lie along lines of constant $\mathbf{q_{xy}}$ and constant $\mathbf{q_z}$; this is indicative of a highly textured crystalline film, with layering in both the xy- and z- planes. We note that for a crystal with finite dimensions, for a small difference 'δ' from the Bragg condition, the plane for which $\delta=(n+1/2)*\lambda$ holds will not be reached. In this case there is not perfect cancellation of the intensity away from the Bragg condition, thus leading to an intensity distribution over small angular range. This can be seen as the path difference of the scattered ray versus the depth of the lattice plane in the crystal. Here we see this as lines of spots which are distinct for incident angles up to 0.19°, above which we begin to see weak Debye-Scherrer rings of intensity at constant $|\mathbf{q}|$ from an increased number of diffracting lattice planes.

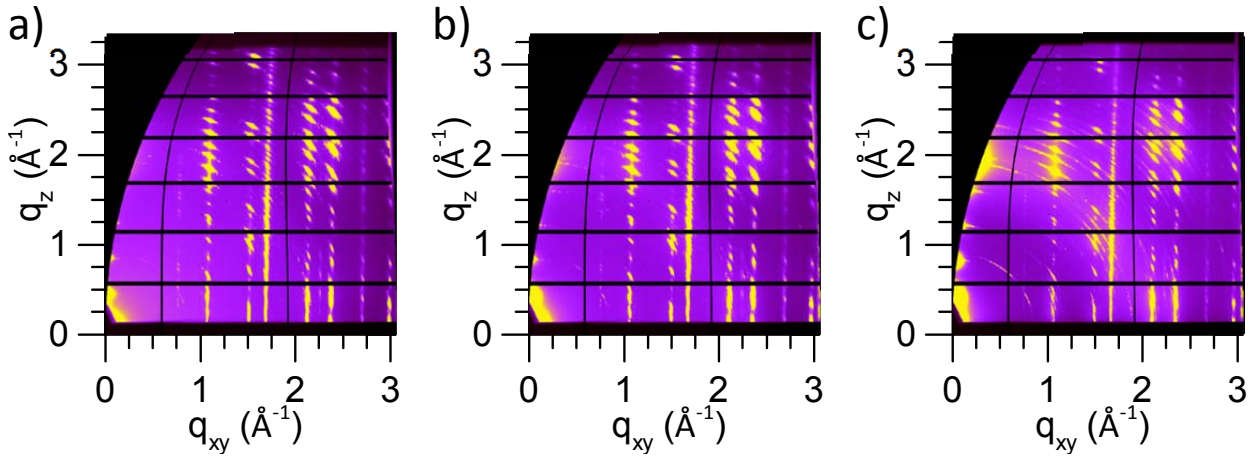

Figure S3. GIWAXS patterns in $\mathbf{q_{xy}}$-$\mathbf{q_z}$ for $(PEA)_2PbI_4$ where the angle of incidence is a) 0.05° b) 0.19° and c) 0.50°. For this material, these angles give attenuation lengths of a) 3 nm, b) 105 nm, and c) 438 nm.

To interpret these patterns, in Figure S4 we compare lines of intensity in the xy-plane (along $\mathbf{q_z} = 0$) and out of the xy-plane (along $\mathbf{q_{xy}} = 0$), with calculated XRD patterns from two simulated structures from the literature which are shown in Figure S5.[6] We expect an increase in the lattice *d*-spacings and a corresponding peak shift towards smaller $|\mathbf{q}|$ for the room temperature GIWAXS data when compared with the simulated patterns (zero Kelvin). In Figure S4 (and Table S2) we see that the out-of-plane peaks occur at smaller $|\mathbf{q}|$ (larger *d*-spacings) only when compared with the staggered structure, where these evenly spaced peaks correspond to the [00*l*] planes. From Table S2 we conclude that the room temperature GIWAXS data is more closely matched to the staggered arrangement of lead iodide octahedra in Figure S5, in agreement with previous literature reports, such that the [00*l*] crystallographic reflections are due to the lead iodide planes lying parallel with the substrate.[6-9]

Further comparison with the simulated pattern of the staggered structure allows identification of peaks in the xy-plane which correspond to [*hk*0] crystallographic directions. Using the Ito method of indexing we find the lattice parameters given in Table S3.[10,11]

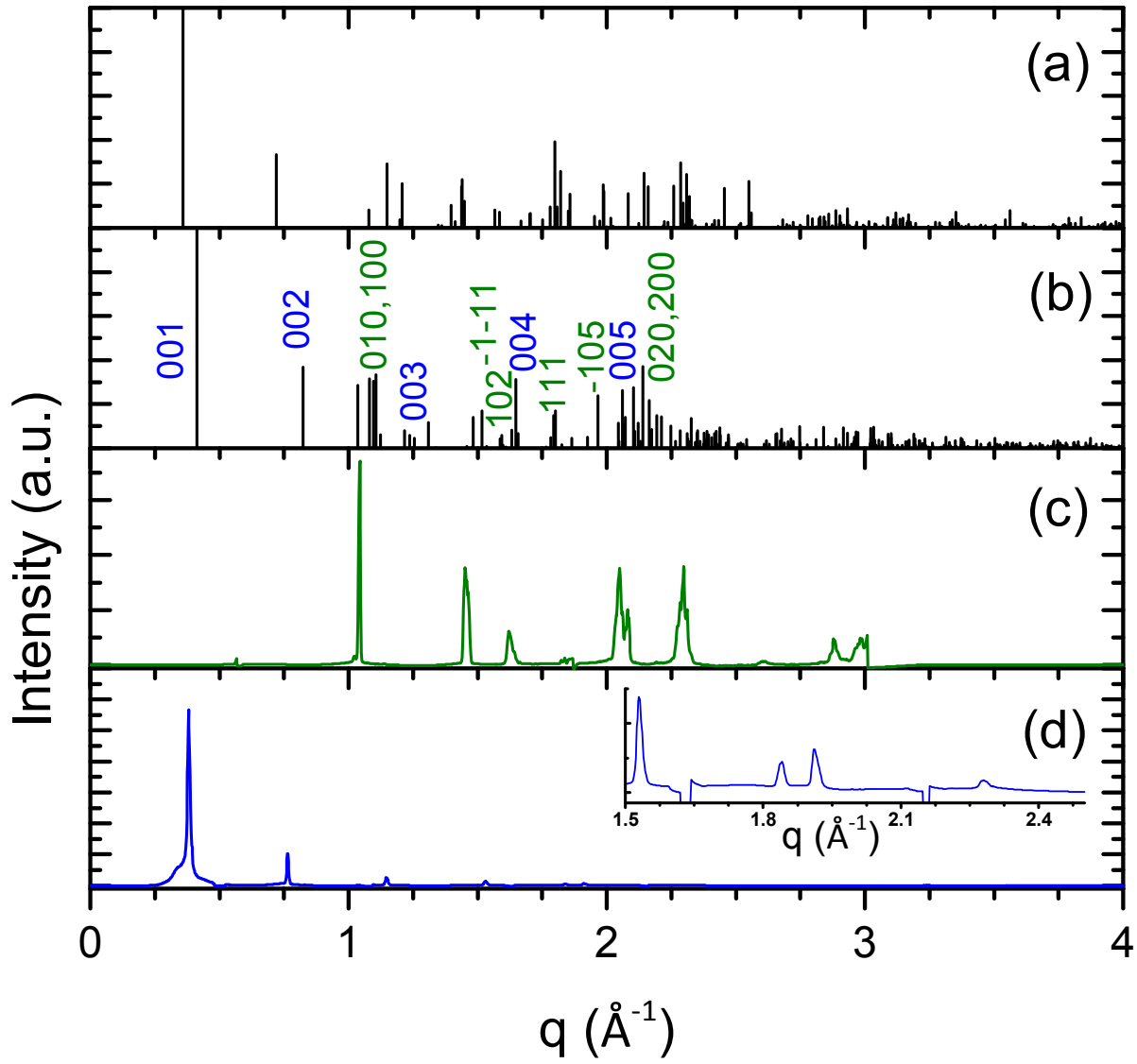

Figure S4. XRD patterns calculated for the (a) eclipsed and (b) staggered structures shown in Figure S5, compared with lines of intensity (c) in plane (along $\mathbf{q}_z = 0$) and (d) out of plane (along $\mathbf{q}_{xy} = 0$) from the GIWAXS pattern in Figure S3.

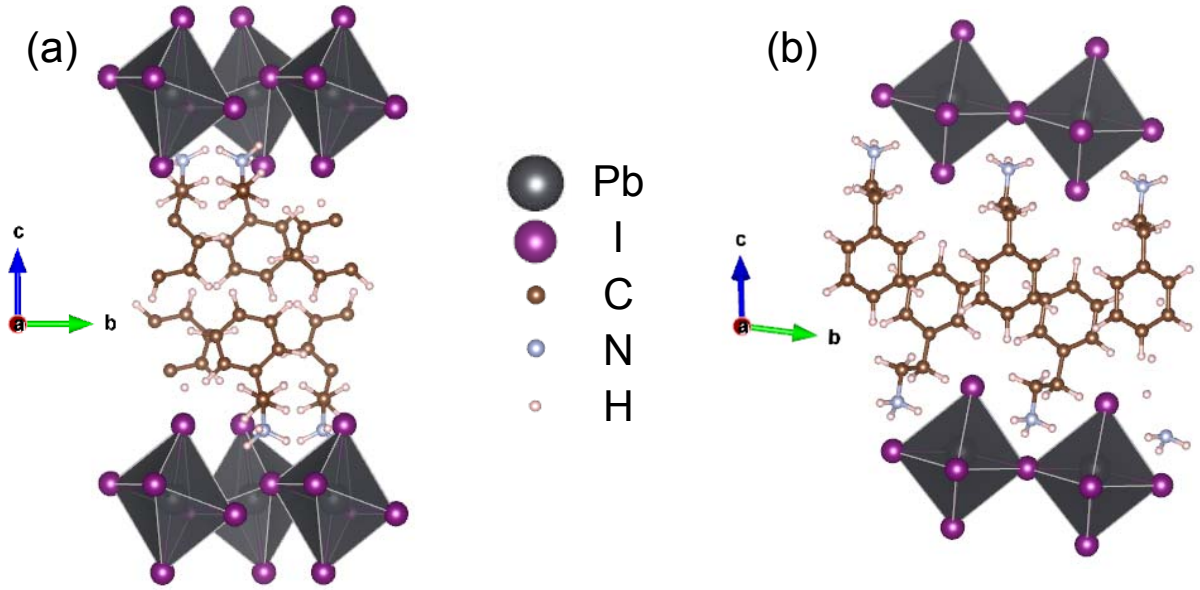

Figure S5. $(PEA)_2PbI_4$ in the (a) eclipsed and (b) staggered structures, visualized in VESTA using the calculated crystal structures by Fraccarollo *et al*.[6]

Table S3. *d*-spacings for [00*l*] lattice planes from simulated and measured structures.[6]

	[001] *d*-spacing (Å)	[002] *d*-spacing (Å)	[003] *d*-spacing (Å)
Simulated Eclipsed	17.4	8.72	5.82
Simulated Staggered	15.2	7.62	5.08
This work (Measured)	15.9	7.92	5.28

Table S4. Lattice parameters for simulated and measured $(PEA)_2PbI_4$.[6]

	a (Å)	b (Å)	c (Å)	α (°)	β (°)	γ (°)	V_{cell} (Å^3)	ρ_{cell} (g cm^{-3})	Space group
Eclipsed	8.98	6.89	17.4	90.0	89.0	90.0	1080.1	1.47	$P2_1/a$
Staggered	6.06	5.88	16.4	97.8	110.1	91.7	542.51	2.94	$P1$
This work	5.92	5.86	16.1	96.2	80.8	91.8	548.77	2.90	$P1$

Densities and Attenuation Lengths

In order to make comparisons between these five material compositions, the beam attenuation lengths in each material must be known. Here the attenuation length is defined as the depth into the material from the surface where the beam intensity drops to 1/*e* of its surface value.

The attenuation lengths for these films depend on the material density. Material densities have been measured for $MAPbI_3$ and $(MA)_2(PEA)_2Pb_3I_{10}$,[12,13] and in the previous section we have determined a density for our $(PEA)_2PbI_4$ films; from these three values we find approximate densities for the other two compositions. We then calculate the beam attenuation lengths as a function of incident angle following Henke *et al.*,[3] which we provide in Figure S6. The relevant parameters for these films are summarised in Table S4. We use Figure S6 to determine the corresponding GIWAXS patterns for a variety of attenuation lengths for comparison in the following section.

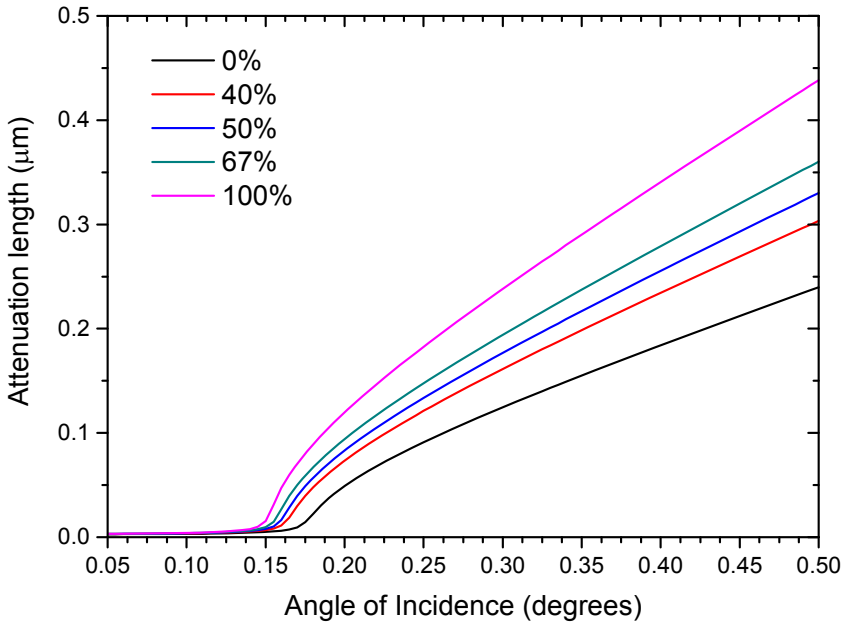

Figure S6. Attenuation lengths for each composition, determined using the densities in Table S4.

Table S5. Approximate densities calculated from experimental and literature values. Angle of incidence for 100 nm attenuation as determined from Figure S6.

% PEA	Material	Density (g cm^{-3})	Angle for 100 nm attenuation (°)
0%	$(MA)PbI_3$	4.2	0.26
40%	$(MA)_3(PEA)_2Pb_4I_{13}$	3.6	0.23
50%	$(MA)_2(PEA)_2Pb_3I_{10}$	3.4	0.22
67%	$(MA)(PEA)_2Pb_2I_7$	3.2	0.20
100%	$(PEA)_2PbI_4$	2.9	0.19

Conventional 'powder' XRD for 2D perovskite films with different PEA content

In Figure S7 we present XRD patterns from films of each composition, which were collected using a Panalytical powder X-ray diffractometer. For each of the MA-containing films, we see a strong diffraction peak at 14° in the powder XRD patterns which is characteristic of the $MAPbI_3$ perovskite. For 67% PEA a second peak appears at lower angles, and additional peaks are visible as the film becomes more oriented (see GIWAXS section). For 100% PEA we observe evenly spaced peaks which correspond to the [00*l*] crystallographic planes as explained previously; we note that with this method of XRD we find only these peaks, which supports the hypothesis of the preferred c-axis orientation, i.e. that the lead-iodide octahedra form layers parallel with the substrate.

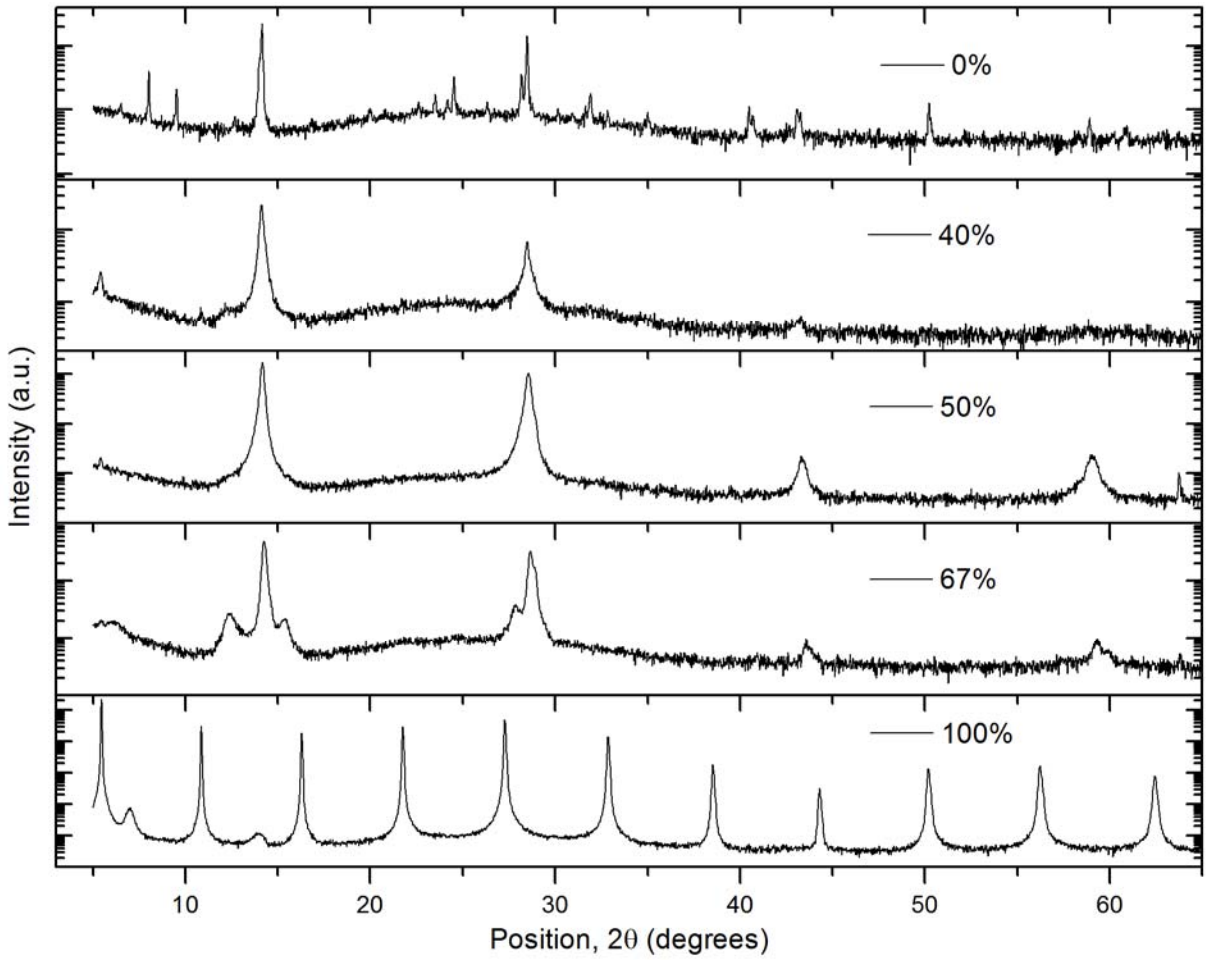

Figure S7. Powder XRD patterns (Cu-$K_{\alpha 1}$) for each material composition, labelled by PEA%.

Depth Dependence of GIWAXS patterns

0% PEA: $MAPbI_3$

Figure S8 shows how the GIWAXS pattern varies with depth into the $MAPbI_3$ film. We see a decrease in peak width with increasing depth, as more planes are contributing to diffraction. Assuming a constant grain size throughout the film, this could also indicate an increase in crystallinity with increasing depth in the film. We note that there are shifts in the positions of major peaks, which we attribute to increased strain in the uppermost surface of the film, although this is convoluted with peak broadening due to the small sample volume. We also observe the disappearance and appearance of peaks with increasing depth as the number of diffraction planes increases. We conclude that the film consists of randomly oriented crystallites of uniform composition throughout the top 240 nm of the film.

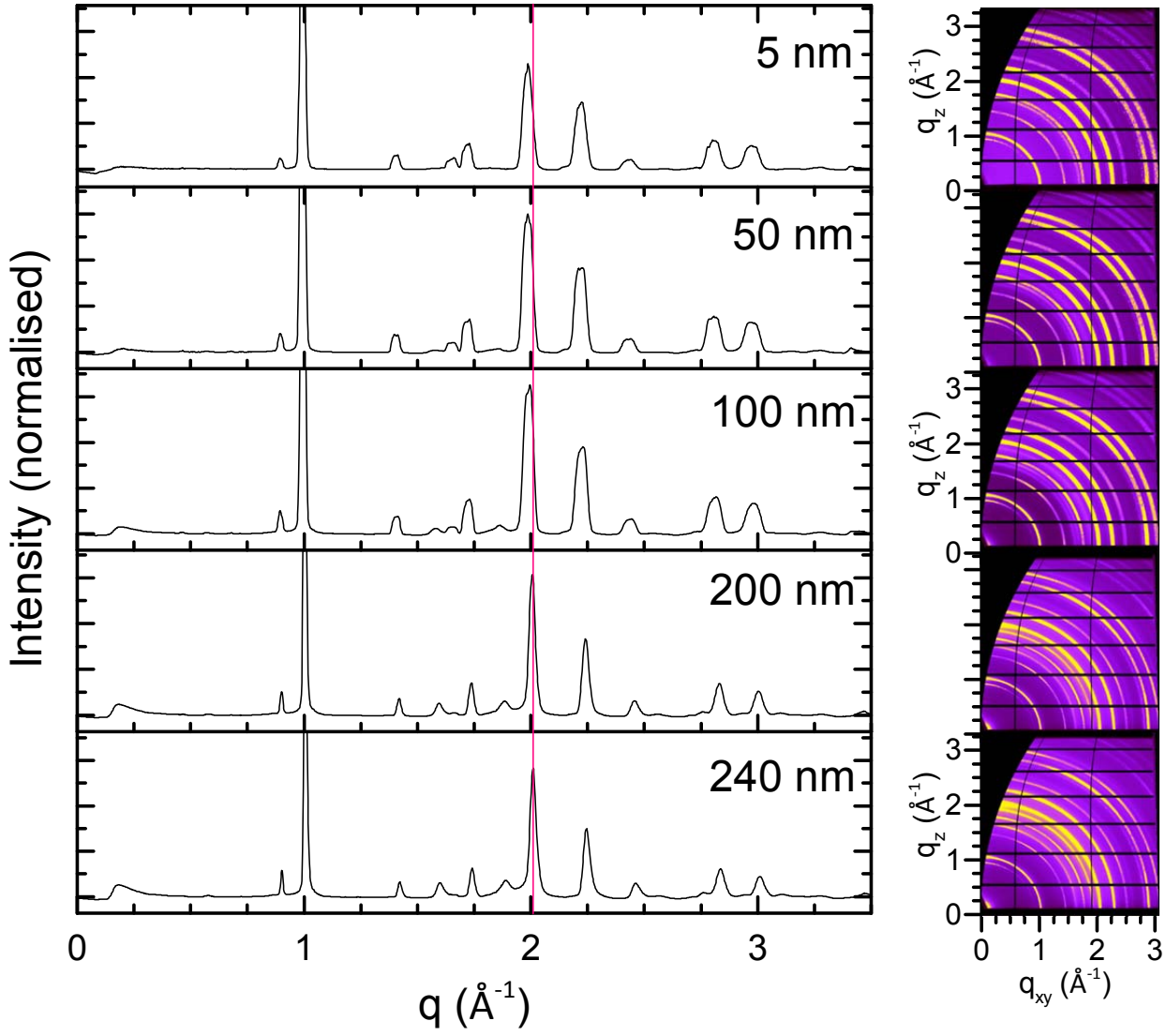

Figure S8. Azimuthal integration (plotted) of GIWAXS patterns in $\mathbf{q_{xy}}$-$\mathbf{q_z}$ (adjacent), for various attenuation lengths from the top of the $MAPbI_3$ film. The intensity is scaled to the second largest peak in order to show the detail of the smaller peaks. Shifting of the peak position is illustrated with a pink line.

40% PEA

Figure S9 shows how the GIWAXS pattern varies with depth into the 40% PEA film. We observe similar patterns for all depths. Most peaks are from Debye-Scherrer rings; there are also a few peaks from intensity in the out of plane direction (see GIWAXS images adjacent). We conclude that the material is uniform throughout the top 300 nm of the film.

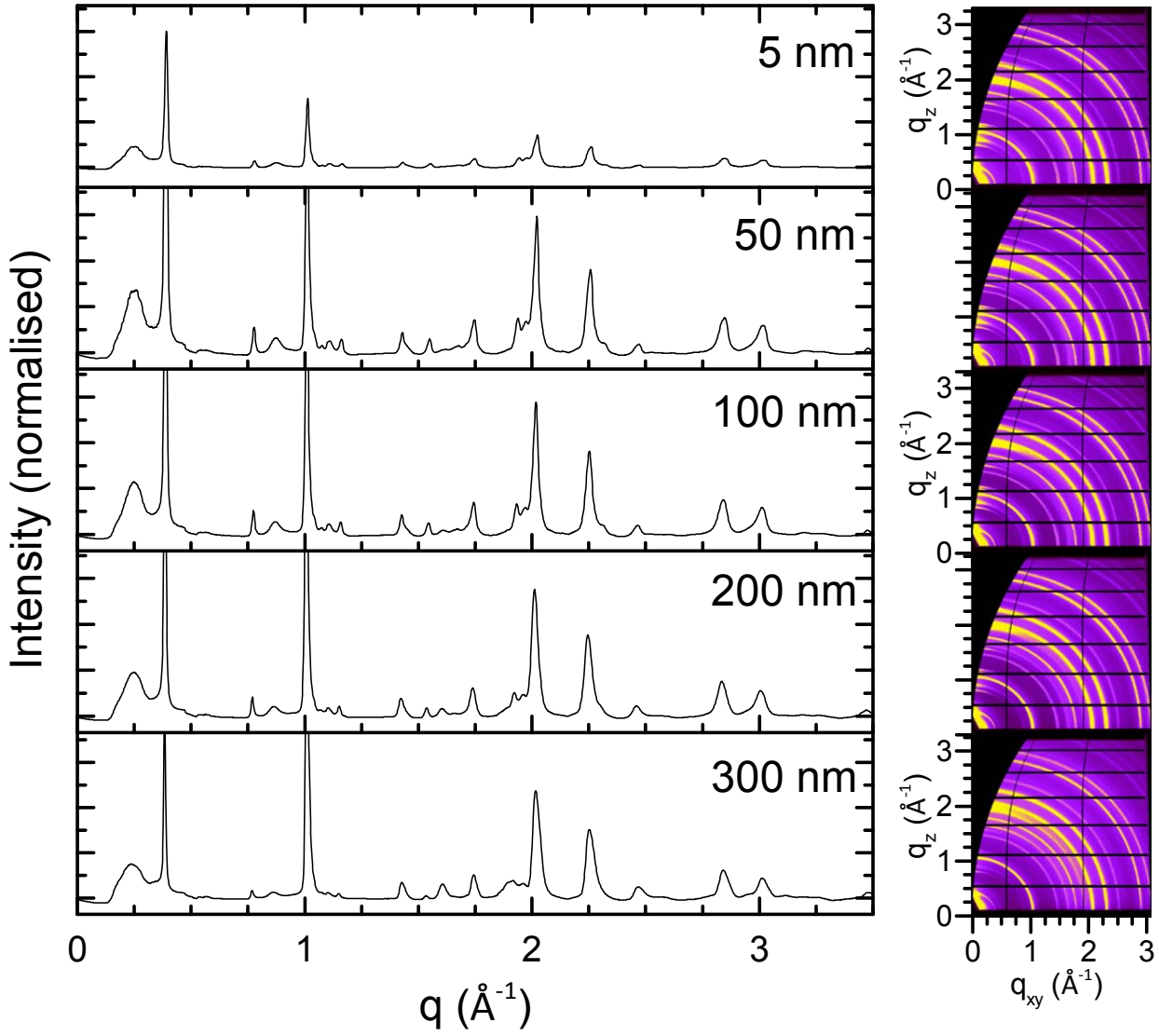

Figure S9. Azimuthal integration (plotted) of GIWAXS patterns in $\mathbf{q_{xy}}$-$\mathbf{q_z}$ (adjacent), for various attenuation lengths from the top of the 40% PEA film. The intensity is scaled to the third largest peak in order to show the detail of the smaller peaks.

50% PEA

Figure S10 shows how the GIWAXS pattern varies with depth into the 50% PEA film. We observe regions of intensity on Debye-Scherrer rings for all depths, with some weak complete rings. The patterns are similar for the uppermost 100 nm; we observe the emergence of some spots of intensity deeper into the film as more diffraction planes are probed. We also note a small decrease in peak width and a slight shift to higher **q** (smaller *d*) with increasing depth for the two main peaks, also due to the increased diffraction planes and/or increased strain near the substrate. We conclude that the material is uniform and takes the same preferential orientation throughout the top 300 nm of the film.

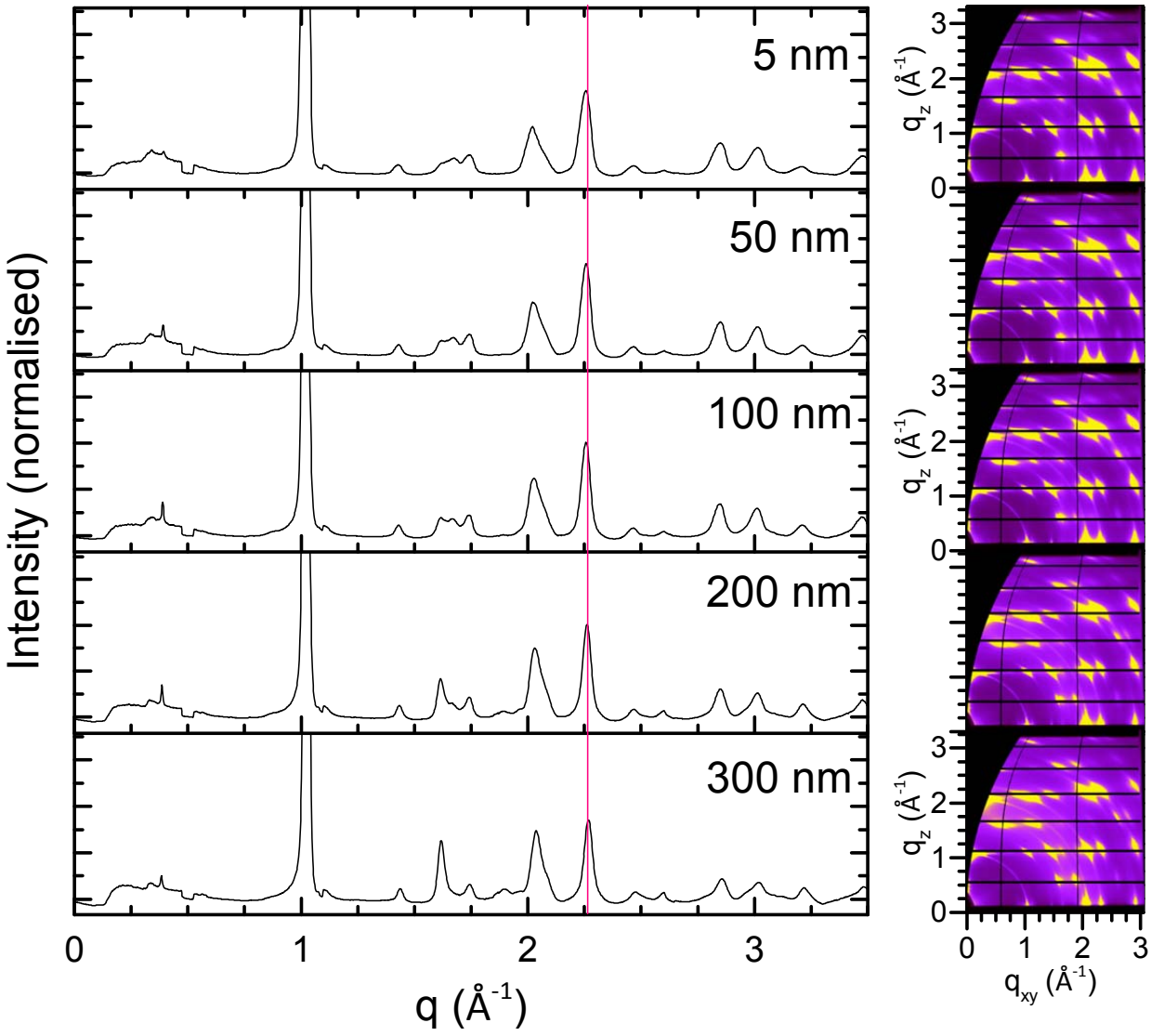

Figure S10 Azimuthal integration (plotted) of GIWAXS patterns in $\mathbf{q_{xy}}$-$\mathbf{q_z}$ (adjacent), for various attenuation lengths from the top of the 50% PEA film. The intensity is scaled to the second largest peak in order to show the detail of the smaller peaks. Shifting of the peak position is illustrated with a pink line.

67% PEA

Figure S11 shows how the GIWAXS pattern varies with depth into the 67% PEA film. We observe regions of intensity on Debye-Scherrer rings for all depths, and also a set of weak complete rings which are strong in the top 5 nm and gradually diminish until they are no longer visible after 100 nm. As in the 50% film, we begin to observe more reflections with increasing depth as an increased number of lattice planes are sampled. Apart from the surface 5 nm, the top 300 nm of the film is uniform in composition and preferential orientation.

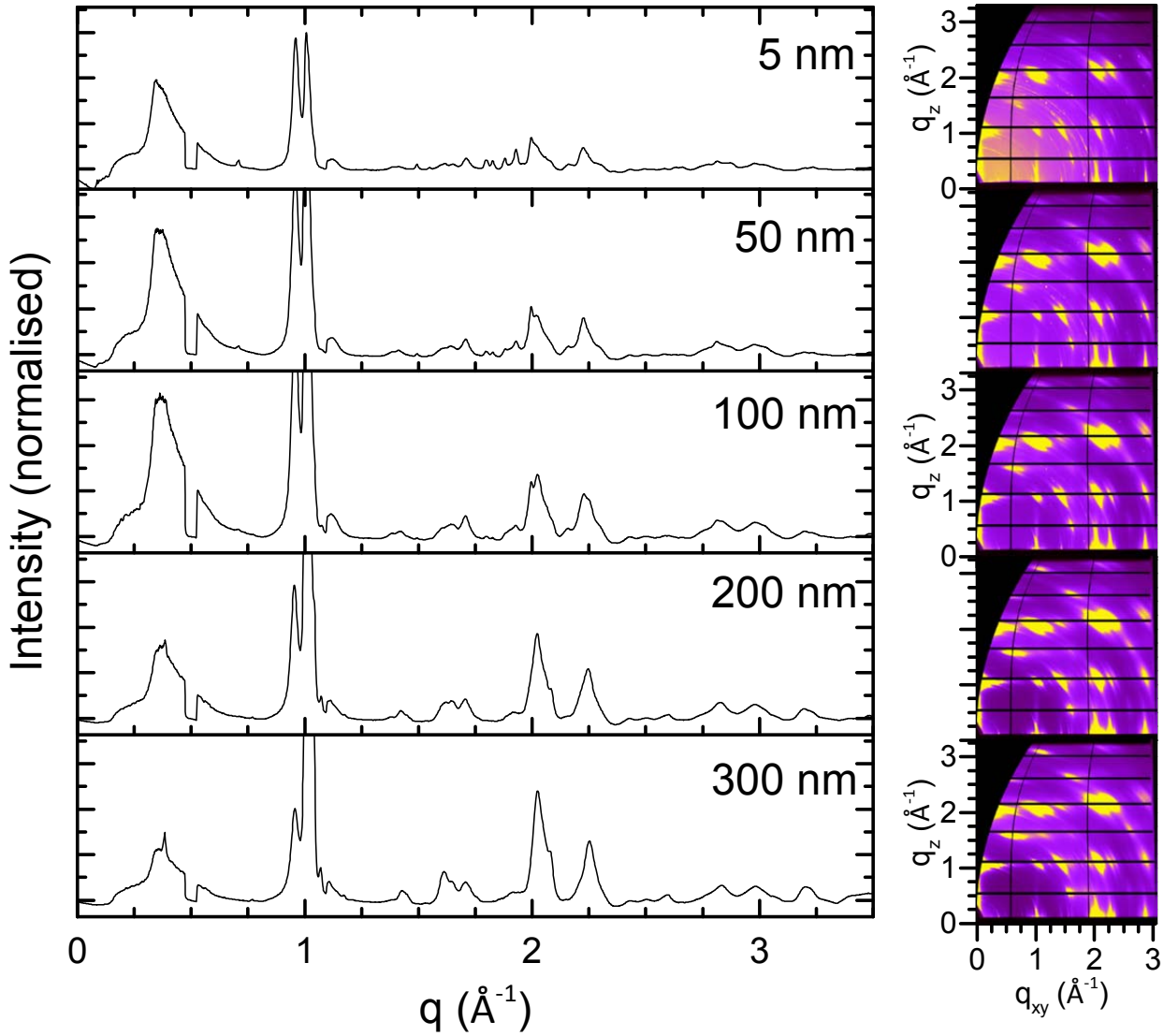

Figure S11 Azimuthal integration (plotted) of GIWAXS patterns in $\mathbf{q_{xy}}$-$\mathbf{q_z}$ (adjacent), for various attenuation lengths from the top of the 67% PEA film. The intensity is scaled to the largest peaks near $|\mathbf{q}| = 2$ in order to show the detail of the smaller peaks.

100% PEA

Figure S12 shows how the GIWAXS pattern varies with depth into the 100% PEA film. As discussed in the Analysis of $(PEA)_2PbI_4$ GIWAXS data section, the Debye-Scherrer rings are broken into sharp spots of intensity which lie along lines of constant $\mathbf{q}_{xy}$ and constant $\mathbf{q}_z$. These lines of spots are distinct for the top 100 nm, below which we see an increase in diffuse scattering attributed to stacking faults deeper in the film. We note that due to layering in both the xy- and z- planes, azimuthal integration gives many small peaks. We conclude that this film is also of uniform composition and preferential orientation throughout the top 438 nm of the film.

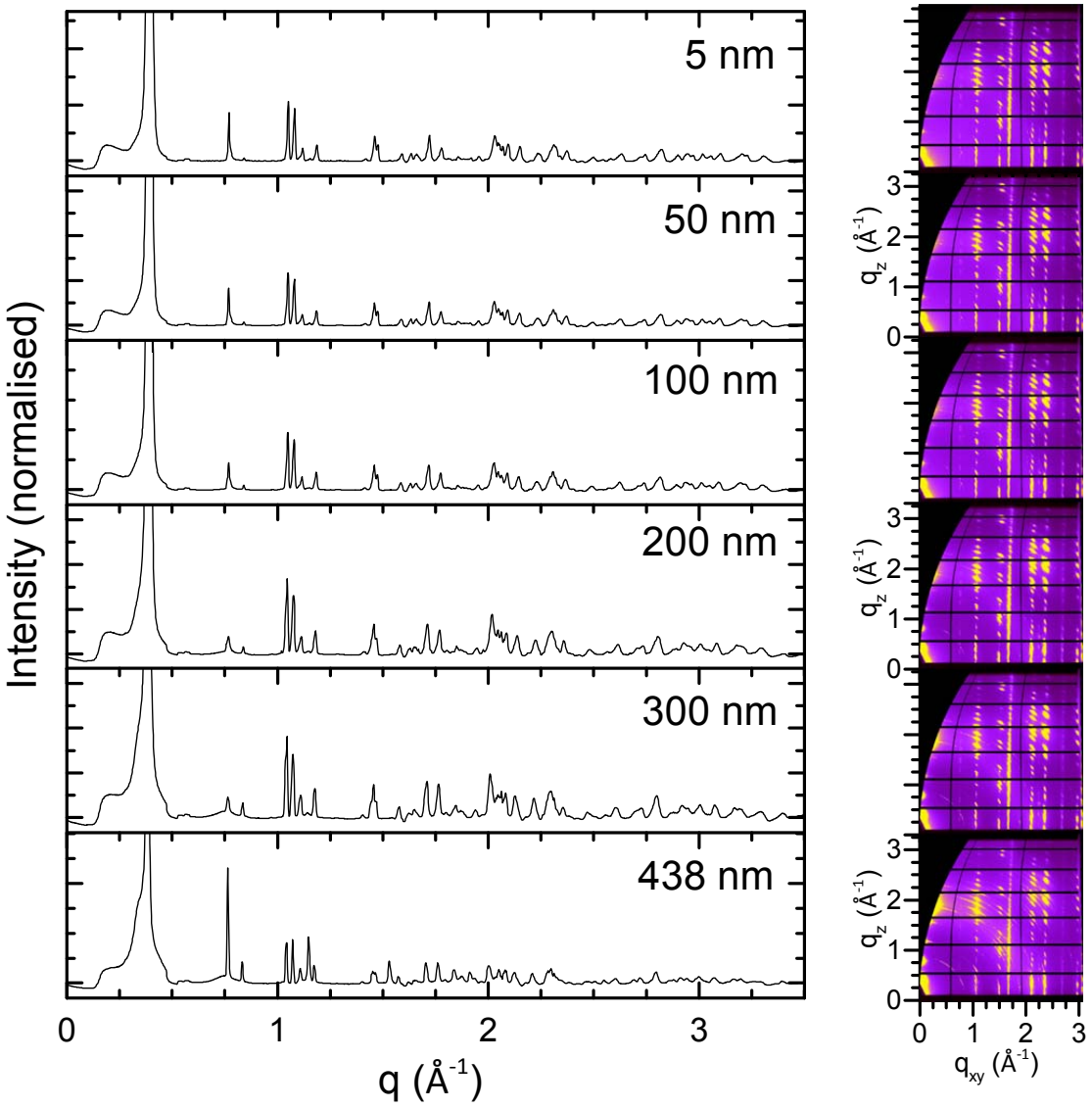

Figure S12 Azimuthal integration (plotted) of GIWAXS patterns in $\mathbf{q}_{xy}$-$\mathbf{q}_z$ (adjacent), for various attenuation lengths from the top of the 100% PEA film. The intensity is scaled to the largest peaks near $|\mathbf{q}| = 2$ in order to show the detail of the smaller peaks.

6. References

(1) Lee, M. M.; Teuscher, J.; Miyasaka, T.; Murakami, T. N.; Snaith, H. J. *Science* **2012**, *338*, 643.
(2) Basham, M.; Filik, J.; Wharmby, M. T.; Chang, P. C. Y.; El Kassaby, B.; Gerring, M.; Aishima, J.; Levik, K.; Pulford, B. C. A.; Sikharulidze, I.; Sneddon, D.; Webber, M.; Dhesi, S. S.; Maccherozzi, F.; Svensson, O.; Brockhauser, S.; Naray, G.; Ashton, A. W. *Journal of Synchrotron Radiation* **2015**, *22*, 853.
(3) Henke, B. L.; Gullikson, E. M.; Davis, J. C. *Atomic Data and Nuclear Data Tables* **1993**, *54*, 181.
(4) Nienhuys, H. K.; Sundström, V. *Phys. Rev. B* **2005**, *71*.
(5) Ulbricht, R.; Hendry, E.; Shan, J.; Heinz, T. F.; Bonn, M. *Rev Mod Phys* **2011**, *83*, 543.
(6) Fraccarollo, A.; Cantatore, V.; Boschetto, G.; Marchese, L.; Cossi, M. *J. Chem. Phys.* **2016**, *144*.
(7) Mitzi, D. B. In *Progress in Inorganic Chemistry, Vol 48*; Karlin, K. D., Ed. 1999; Vol. 48, p 1.
(8) Cheng, Z. Y.; Wang, Z.; Xing, R. B.; Han, Y. C.; Lin, J. *Chem. Phys. Lett.* **2003**, *376*, 481.
(9) Zhang, S. J.; Audebert, P.; Wei, Y.; Al Choueiry, A.; Lanty, G.; Brehier, A.; Galmiche, L.; Clavier, G.; Boissiere, C.; Lauret, J. S.; Deleporte, E. *Materials* **2010**, *3*, 3385.
(10) Ito, T. *Nature* **1949**, *164*, 755.
(11) Ito, T. *X-Ray Studies on Polymorphism*; Maruzen: Tokyo, 1950.
(12) Stoumpos, C. C.; Malliakas, C. D.; Kanatzidis, M. G. *Inorg. Chem.* **2013**, *52*, 9019.
(13) Smith, I. C.; Hoke, E. T.; Solis-Ibarra, D.; McGehee, M. D.; Karunadasa, H. I. *Angew. Chem.-Int. Edit.* **2014**, *53*, 11232.